Supporting Information for "Imaging the Kanto Basin bedrock with noise and earthquake autocorrelations"

Loïc Viens[1], Chengxin Jiang[2], and Marine A. Denolle[3]

[1]Disaster Prevention Research Institute, Kyoto University, Uji, Japan

[2]Research School of Earth Sciences, The Australian National University, Canberra, ACT, Australia

[3]Department of Earth and Planetary Sciences, Harvard University, Cambridge, MA, USA

Contents of this file

1. Texts S1 to S6
2. Figures S1 to S6
3. Tables S1 and S2

Corresponding author: Loïc Viens, Disaster Prevention Research Institute, Kyoto University, Uji, Japan (viens.loic.58r@st.kyoto-u.ac.jp)

Introduction

The supporting information includes:

1. Text and Figure S1 discussing the seasonal stability of the noise autocorrelation functions (ACFs)

2. Text and Figure S2 showing the effect of the average trace removal for the stations along Line 1

3. Text and Figure S3 showing the effect of the length of the sliding-spectral windows on earthquake ACFs.

4. Text and Figure S4 showing noise and earthquake ACFs with clipped amplitudes along Line 4

5. Text and Figure S5 showing the noise and earthquake ACFs in the 0.33-1 s (1-3 Hz) period range

6. Table S1 showing the station names and locations for which the noise ACF $2p^3$ values are manually picked

7. Text and Figure S6 and Table S2 showing the results of the 2-D SOFI2D simulations.

Text S1.

To demonstrate the stability of noise ACFs with seasonality, we independently stack the 20-min ACFs for the 2-week periods of January and July with the phase-weighted stack (PWS) method (Schimmel & Paulssen, 1997). We show the noise ACFs as well a the selected negative peak values between the theoretical $2p^3$ phase ± 2.5 s from the JIVSM for the stations along Line 1 in Figure S1. The P-wave two-way travel times obtained

independently from the January and July data are consistent with that from the stack over the entire dataset.

We also compare the difference between the JIVSM and January/July noise ACF bedrock depths over the entire network after migrating the P-wave two-way travel times from the noise ACFs to depth using a constant P-wave velocity of 2.53 km/s (e.g., average of the surface-to-bedrock P-wave velocity from the JIVSM over the 287 station locations). For the January noise ACFs, the mean of the depth difference with the JIVSM (μ) is -0.09 km and the one standard deviation (σ) is 0.28 km. For the July noise ACFs, μ is equal to -0.12 km and σ is 0.29 km. These values are very similar to that obtained with the stack over the entire dataset shown in the main manuscript ($\mu = -0.091$ km and $\sigma = 0.290$ km), confirming that noise ACFs are relatively stable through the year.

Text S2.

In Figure S2, we show the effect of the average trace removal on the noise ACFs for the stations along Line 1. The raw noise ACFs are primarily dominated by the near zero-time-lag spikes. By removing an average trace to each ACF, we remove the effect of the source function and enhance the signal-to-noise ratio of the reflectivity response.

Text S3.

Earthquake spectra are pre-whitened using the running-mean average algorithm of Bensen et al. (2007) before computing earthquake ACFs. In the main manuscript, we present the results using a sliding-spectral window of 30 samples (i.e., 0.67 Hz). In the

Supplementary material, we also compute earthquake ACFs with sliding-spectral window of 20 and 45 samples. For the 20-, 30-, and 45-sample sliding-spectral windows, we first measure the two-way travel times from the earthquake ACFs within the theoretical 2p arrival time ± 0.65 s time window. We then migrate the two-way travel times to depth using a constant P-wave velocity of 2.53 km/s and show the bedrock depth maps in Supplementary Material Figure S3. The maps have similar bedrock depths and similar lateral variations. For the 20- and 45-sample sliding-spectral windows, the means of the depth residuals with the JIVSM (μ) are 0.057 km and 0.085 km and the standard deviations to the mean (σ) are 0.334 km and 0.314 km, respectively. These values are very similar to that obtained with a 30-sample sliding-spectral window ($\mu = 0.085$ km and $\sigma = 0.327$ km), which confirms that the degree of smoothing does not significantly impact our results. Finally, a 30-sample sliding-spectral window allows us to measure the 2p travel time at more stations (e.g., 270 out of 287 stations) than if 20- or 45-sample sliding-spectral windows are used (e.g., 259 and 268 out of 287 stations, respectively).

Text S4.

In Figure S4, we show the noise and earthquake ACFs along Line 4 and clip their amplitudes for visibility. In Figure S4b, a clear consistent phase near the theoretical $2p^3$ phase can be observed along Line 4 after clipping the waveforms amplitudes, which is not the case in Figure 3f of the main manuscript. Moreover, several negative peaks can be observed within the theoretical $2p^3 \pm 2.5$ s time window between 20 to 50 km from the south-western end of Line 4. In the main manuscript, we automatically select the negative

peaks that are the closest to the theoretical $2p^3$ phase. In Figures S4b and S4d, we show that by selecting ∼0.5 to 1 s earlier negative peaks, the resulting P-wave two-way travel times are very similar to that obtained from the earthquake ACFs. This indicates that the basin bedrock could be up to 1.3 km shallower than that predicted by the JIVSM in this region by considering a constant P-wave velocity of 2.53 km/s.

Text S5.

In Figure S5, we show the noise and earthquake ACFs in the 0.33 to 1 s period range (e.g., 1–3 Hz) at the stations along Lines 3 and 4. For both methods, the only difference with the main manuscript is the frequency range of the bandpass filter applied after autocorrelating and stacking the waveforms. The high-frequency noise ACFs do not show any clear phases near the theoretical 2p, $2p^2$, and $2p^3$ arrival times. On the other hand, the high-frequency earthquake ACFs have clear arrivals near the theoretical 2p arrival time in some parts of the basin (e.g., mainly where the four lines intersect), but are noisier than in the 1 and 10 s period range.

Text S6.

To explain the presence (or absence) of the multiples observed at some stations in the noise and earthquake ACFs, we simulate the elastic wave propagation in layered 2-dimensional media with the finite difference modeling SOFI2D package (Figure S6, Bohlen et al., 2016). The velocity models are taken from the JIVSM at the location of the HYHM

and STHM stations, which are located above relatively flat sedimentary layers to limit the unwanted contributions from 3-D wave propagation effects.

The two velocity models are shown in Figures S6a and S6e and detailed in Table S2. Note that the top boundary is the free surface and the sides and bottom (depth: 25 km) of the model have perfectly matched layers to damp the waves and avoid reflections. For the two models, a receiver is located at a depth of 20 meters. To simulate the noise and earthquake ACFs, we use Ricker source functions with a dominant frequency of 2 Hz (0.5 s) located at two different depths: 20 m to reproduce the noise ACF and 20 km to reproduce the earthquake ACF and simulate the near vertical incidence of teleseismic P waves.

The waveforms of the deep and surface sources recorded at the station for the two velocity models are shown in Figures S6b and S6f. For the HYHM and STHM stations, we bandpass filter the synthetic waveforms between 4 and 10 s and 3 and 10 s, respectively. We focus on slightly different period ranges as the noise and earthquake ACFs at the two stations have different predominant period ranges, with the ACFs at the HYHM stations having a lower frequency content compared to that at the STHM station.

In the following, the 40-s waveform recorded at the surface station is considered for the deep source as earthquake ACFs contain the direct P-waves and their coda. For the shallow source, however, we only consider the part of the waveforms after approximately 9 s (after the green dashed lines in Figure S6b and S6f), as the ambient noise generally does not contain any strong direct arrivals. The considered synthetic waveforms are then autocorrelated in the frequency domain after zero-padding them to four times their

original duration. Finally, we taper the first 0.5 s of the causal part of the simulated ACFs and normalize their amplitudes.

We show the simulated with the deep source and earthquake ACFs for the two stations in Figures S6c and S6g. For both stations, the simulated ACFs reproduce relatively well the earthquake ACFs. The first negative peak of the earthquake ACFs (Figures S6c and S6g), which corresponds to the 2p arrival time, is well retrieved. Moreover, the following positive peak, which we attribute to the $2p^2$ arrival time in the main manuscript, is also retrieved. More interestingly, the higher frequency content of the ACF at the STHM station makes the $2p^2$ phase appear more clearly compared to that at the HYHM station. This is coherent with the earthquake ACFs at the two stations, with the earthquake ACF at the STHM station having a stronger $2p^2$ phase compared to that at the HYHM station. Therefore, the difference of layer thickness and the bedrock depth can explain the presence (or absence) of P-wave multiples in the earthquake ACFs through a different frequency content.

In Figures S6d and S6h, we show the simulated with the surface source and noise ACFs for the two stations. Similarly to the earthquake ACFs, the simulated ACFs reproduce well the noise ACFs at the two stations and the $2p^3$ phase is also well retrieved. Moreover, the simulated ACF at the HYHM station has fewer multiples than that at the STHM station, which is consistent with the noise ACFs. For both stations, the noise ACF phases are also slightly delayed compared to that of the simulations, which is consistent with the slightly delayed measured P-wave two-way travel times shown in Figure 2h.

While the simulated ACFs reproduce well the noise and earthquake ACFs, some differences in terms of both phase and amplitude of the waveforms can be observed, which we can be attributed to following factors. 1) The layered 2-D velocity models might be too simple and do not capture 3-D wave propagation effects. 2) The internal layering from the JIVSM (above the seismic basement) may not be accurate enough.

References

Bensen, G. D., Ritzwoller, M. H., Barmin, M. P., Levshin, A. L., Lin, F., Moschetti, M. P., ... Yang, Y. (2007). Processing seismic ambient noise data to obtain reliable broad-band surface wave dispersion measurements. *Geophys. J. Int.*, *169*, 1239–1260. doi: 10.1111/j.1365-246X.2007.03374.x

Bohlen, T., Nil, D. D., Köhn, D., & Jetschny, S. (2016). *Sofi2d seismic modeling with finite differences: 2d – elastic and viscoelastic version* (used under GNU General Public License, Free Software Foundation). Karlsruhe Institute of Technology.

Schimmel, M., & Paulssen, H. (1997, 08). Noise reduction and detection of weak, coherent signals through phase-weighted stacks. *Geophys. J. Int.*, *130*, 497-505. doi: 10.1111/j.1365-246X.1997.tb05664.x

Table S1: List of stations where the negative peaks of noise ACF near the theoretical $2p^3$ arrival time are manually adjusted.

Station name	Latitude	Longitude
KMHM	35.37081	139.51450
KSGM	35.72642	139.78508
KYTM	35.55539	140.18094
NBKM	35.95800	140.58061
SMGM	35.38658	139.52344
TMHM	35.51506	140.15281
YYIM	35.71855	139.76035

Table S2: Details of the two velocity models used in Figure S6. The "JIVSM layer depth" column shows the depth of the top and bottom of each layer in kilometers. The "used layer depths" are slightly different due to computational constrains. Vp, Vs, and ρ are the P-wave and S-wave velocities and the density of each layer, respectively.

Model	JIVSM layer depth (km)	Used layer depth (km)	Vp (km/s)	Vs (km/s)	ρ (g/cm^3)
Model 1 HYHM station	0.00–0.400	0.00–0.40	1.8	0.5	1.95
	0.400–1.455	0.40–1.46	2.3	0.9	2.1
	1.455–2.667	1.46–2.67	3.0	1.5	2.25
	2.667–25.000	2.67–25.00	5.5	3.2	2.65
Model 2 STHM station	0.0–0.420	0.0–0.42	1.8	0.5	1.95
	0.420–1.104	0.42–1.10	2.3	0.9	2.1
	1.104–1.788	1.10–1.78	3.0	1.5	2.25
	1.788–25.000	1.78–25.00	5.5	3.2	2.65

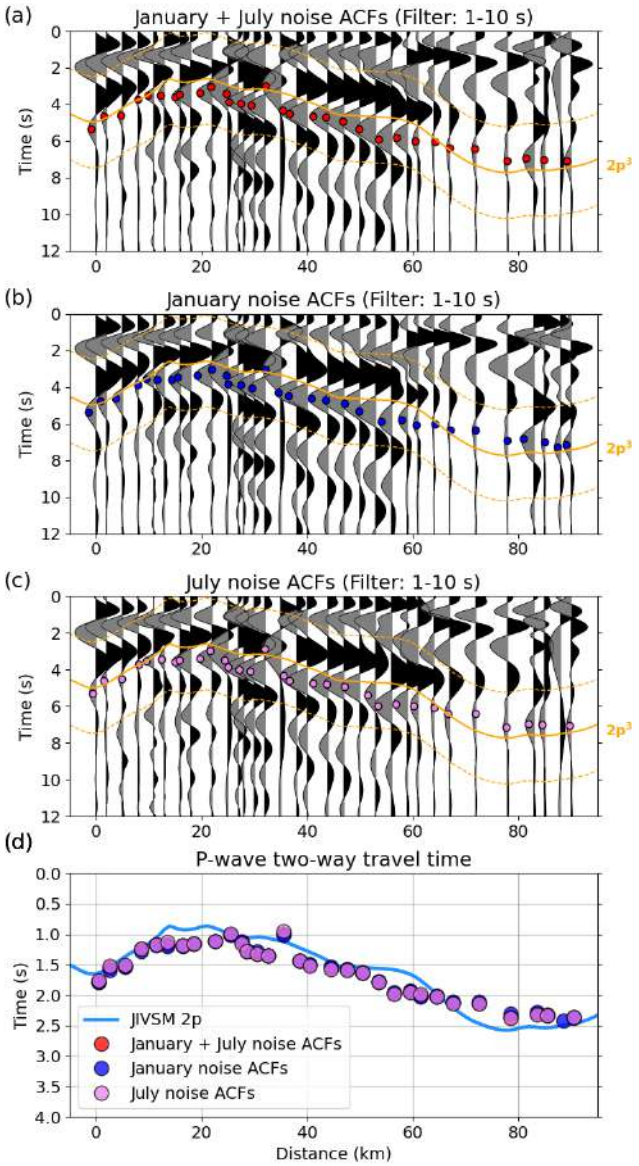

Figure S1: Noise ACFs along Line 1 computed from the data recorded in (a) January and July (e.g., main manuscript), (b) January, and (c) July. All the ACFs are bandpass filtered between 1 and 10 s and an average trace has been subtracted to each ACF to enhance the reflectivity response. The thick orange lines represent the theoretical $2p^3$ arrivals from the JIVSM and the dashed orange lines are the $2p^3$ arrivals ± 2.5 s. The selected negative peaks are shown by the red, blue, and purple filled circles. (d) Theoretical P-wave two-way travel time from the JIVSM (2p, blue line) and the values obtained from (a), (b), and (c) divided by 3 (colored circles).

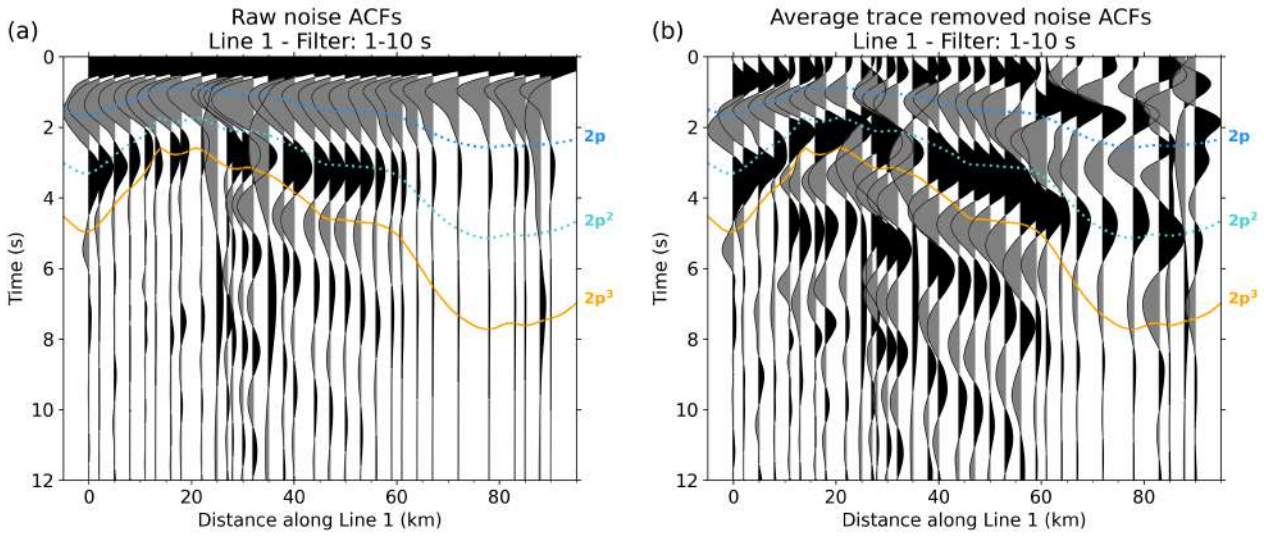

Figure S2: (a) Raw noise ACFs along Line 1 computed over the 30 days of continuous vertical records. (b) Noise ACFs along Line 1 after removing an average trace to each noise ACF. All the waveforms are normalized by their peak absolute amplitude. The amplitude of the waveforms in (a) is 3 times that of the waveforms in (b) for visibility. The blue, light blue, and orange lines represent the theoretical 2p, $2p^2$, and $2p^3$ arrival times from the JIVSM. All the ACFs are bandpass filtered between 1 and 10 s.

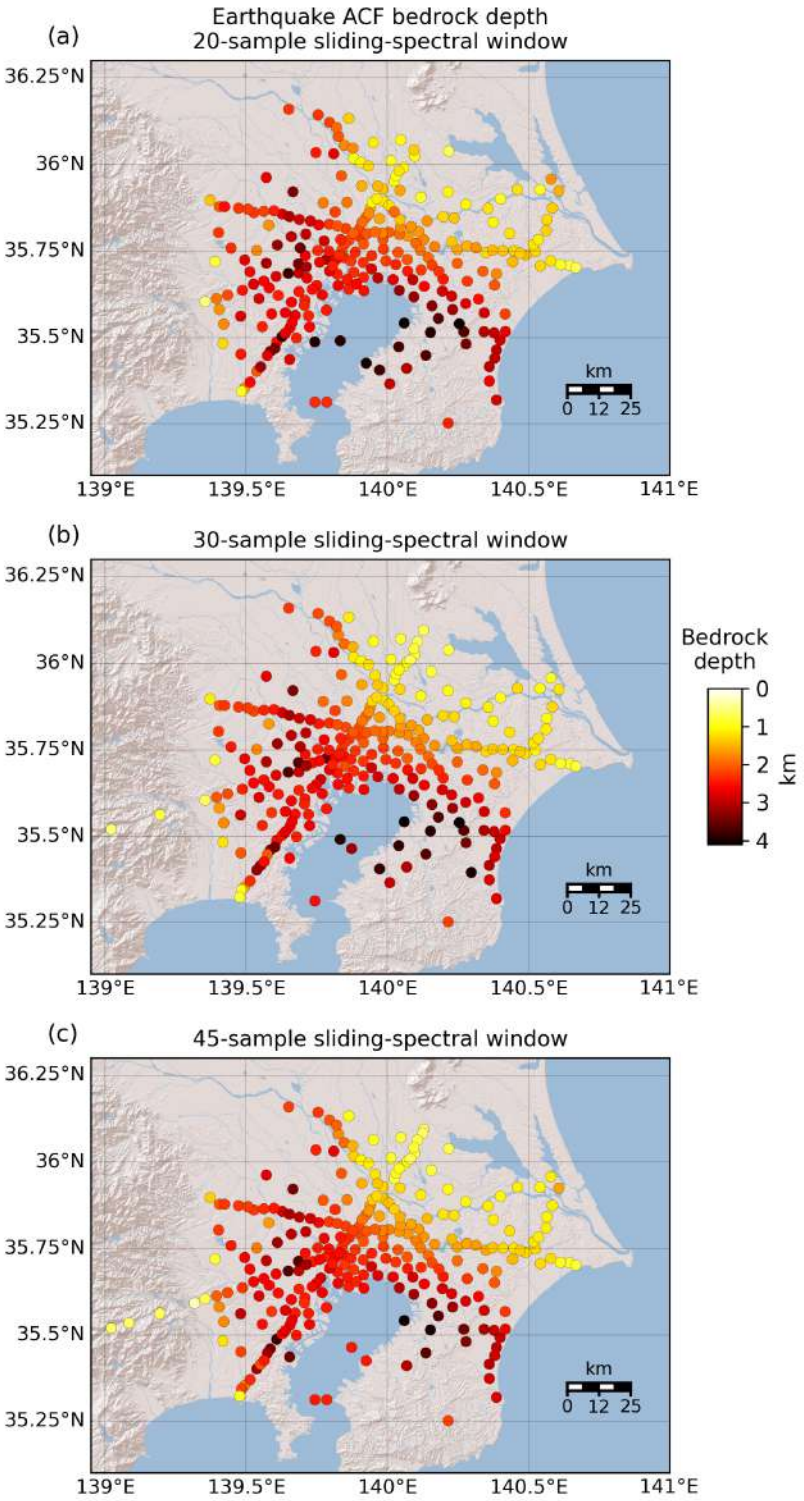

Figure S3: Earthquake ACF bedrock depths obtained with pre-whitening sliding-spectral windows of (a) 20-, (b) 30-, and (c) 45-samples. The bedrock depths are obtained by migrating the two-way travel times measured from earthquake ACFs to depth using a constant P-wave velocity of 2.53 km/s. Note that 259, 270, and 268 stations (out of 287) are used in (a), (b), and (c), respectively, as some waveforms do not contain any negative peaks within the theoretical 2p arrival time ±0.65 s time window.

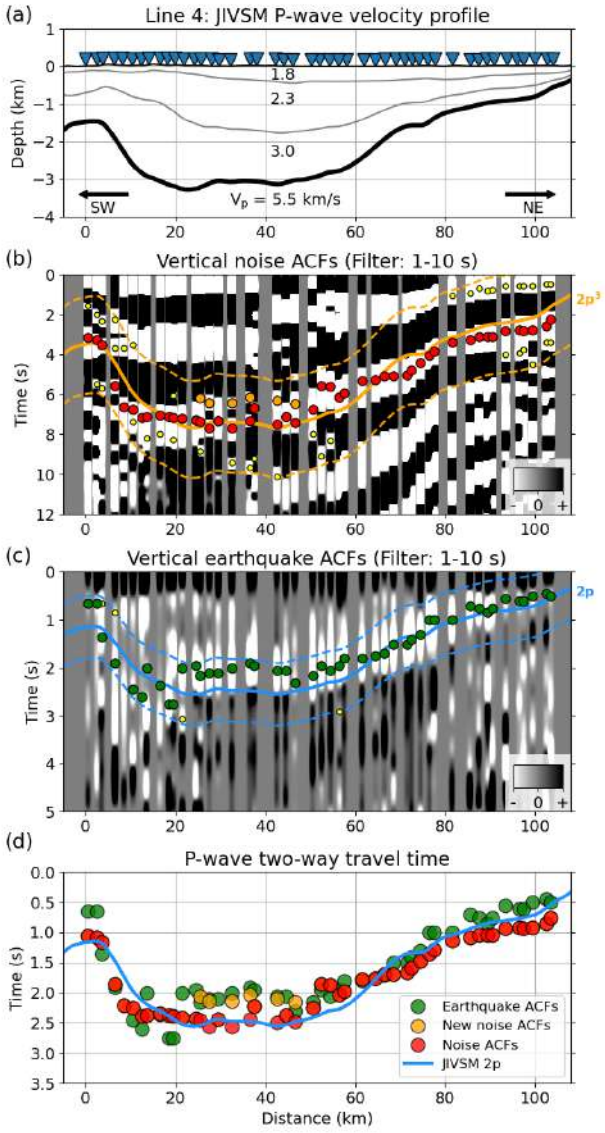

Figure S4: (a) JIVSM P-wave velocity profile along Line 4. (b) Noise ACFs along Line 4 bandpass filtered between 1 and 10 s with clipped amplitudes for visibility. The orange thick and dashed lines highlight the theoretical $2p^3$ arrival time and the $2p^3$ arrival ± 2.5 s, respectively. The red and orange filled circles are the negative peaks used in the main manuscript and in the Supplementary Material Text S4, respectively. The yellow filled circles are other negative peaks found within the theoretical $2p^3$ arrivals ± 2.5 s window. (c) Vertical earthquake ACFs filtered between 1 and 10 s with clipped amplitudes for visibility. The blue line represents the theoretical 2p arrival time and the dashed lines are the blue line $\pm$ 0.65 s. The green dots are the negative peaks selected within the considered time window. Note that the vertical time axes in (b) and (c) are different. (d) Theoretical P-wave two-way travel time (2p, blue line), measured 2p travel time from earthquake ACFs (green circles), measured noise ACF values within the theoretical $2p^3 \pm 2.5$ s window divided by 3 (red circles, used in the main manuscript), and early noise ACF measurements discussed in Supplementary Material Text S4 (orange circles).

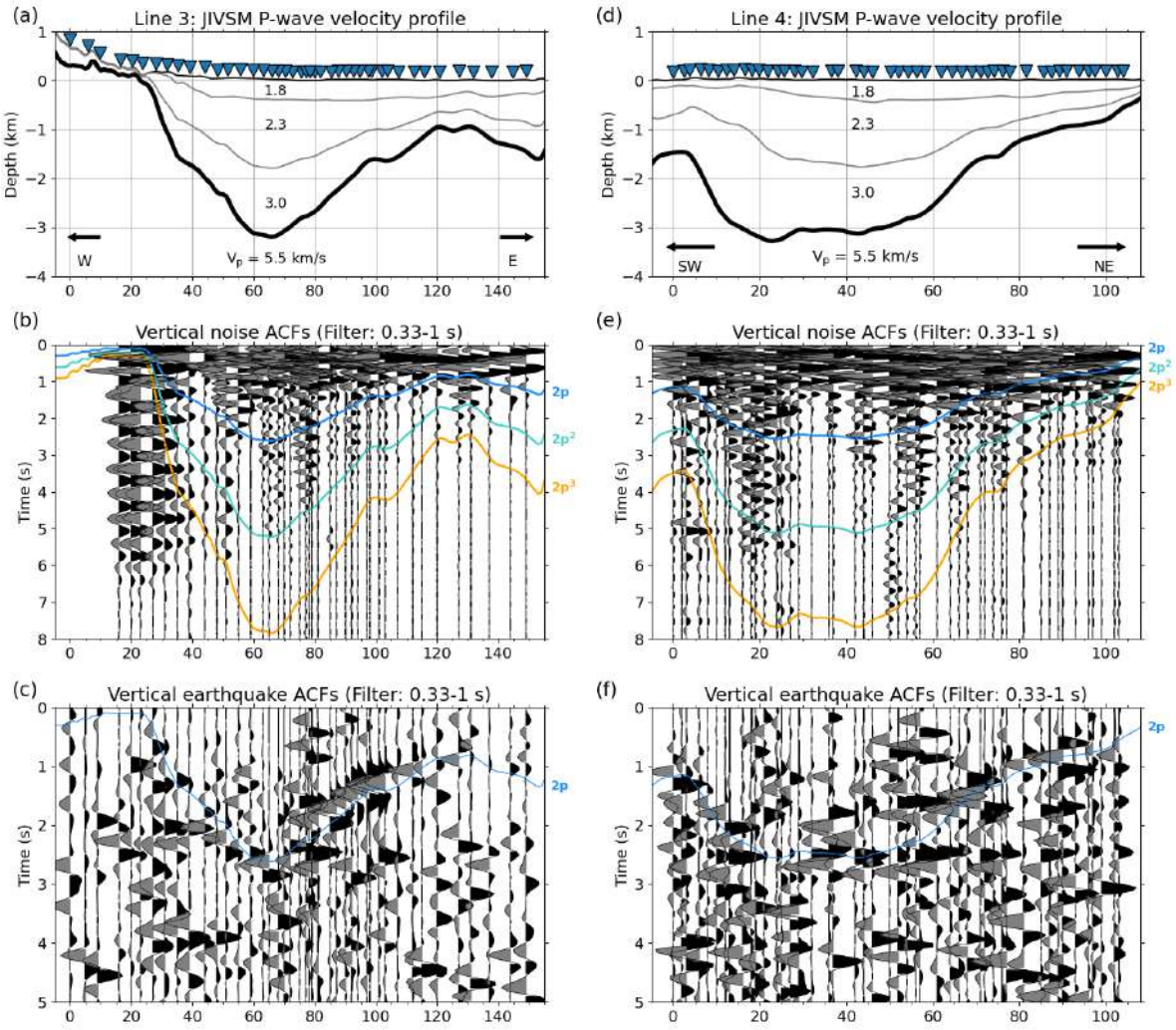

Figure S5: (a) JIVSM P-wave velocity profile along Line 3. (b) Noise ACFs bandpass filtered between 0.33 and 1 s (1-3 Hz) for the stations along Line 3. The theoretical 2p, $2p^2$, and $2p^3$ arrival times from the JIVSM are also highlighted. (c) Earthquake ACFs bandpass filtered between 0.33 and 1 s (1-3 Hz) for the stations along Line 3. (e-f) Same as (a-c) for the stations along Line 4.

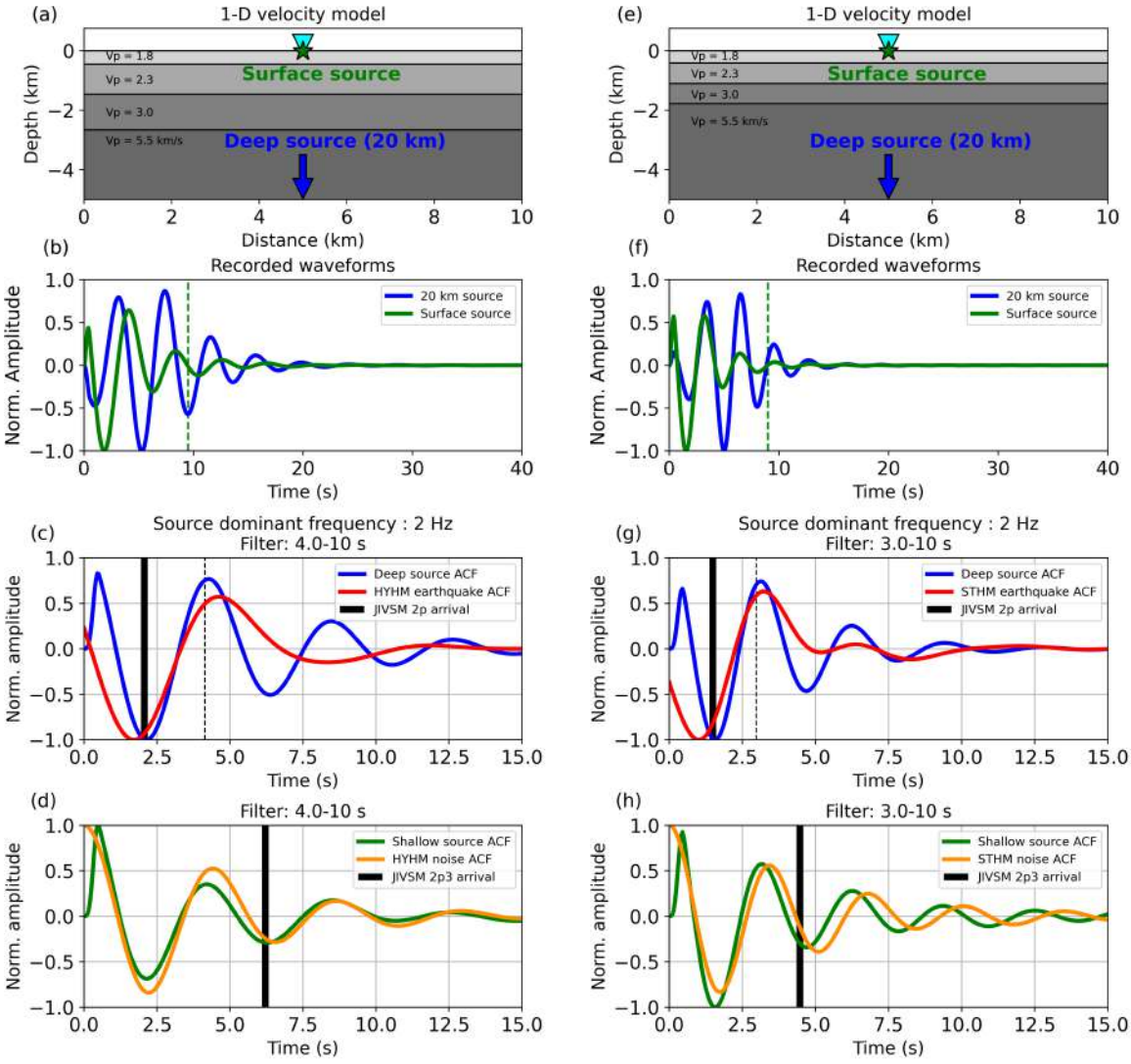

Figure S6: (a) 2-D velocity model used for the SOFI2D simulations at the HYHM station, including the surface and deep source locations of the Ricker functions (green start and blue arrow) and the recording station (inverted blue triangle). (b) Recorded waveforms from the surface and deep sources at the station (green and blue traces). For the surface source, only the part of the waveform after the vertical green dashed line is considered to compute the simulated ACF shown in (d). (c) ACF of the simulated waveform from the deep source (blue trace), earthquake ACF at the HYHM station (red trace), and theoretical 2p and $2p^2$ arrival times (vertical black thick and dashed lines) from the JIVSM calculated from the 2-D velocity model in (a). (d) ACF of the simulated waveform from the shallow source (green trace), noise ACFs at the HYHM station (orange trace), and theoretical $2p^3$ arrival from the JIVSM from the 2-D velocity model in (a). (e-h) Same as (a-d) for the velocity model below the STHM station. Note that the period range in (g) and (h) is slightly different from that in (c) and (d).